Ductile fracture locus identification using mesoscale critical equivalent plastic strain

Xin, Haohui; Veljkovic, Milan; Correia, José A.F.O.; Berto, Filippo

DOI
10.1111/ffe.13429

Publication date
2021

Document Version
Final published version

Published in
Fatigue and Fracture of Engineering Materials and Structures

Received: 11 October 2020 | Revised: 28 December 2020 | Accepted: 22 January 2021

DOI: 10.1111/ffe.13429

ORIGINAL CONTRIBUTION

FFEMS Fatigue & Fracture of Engineering Materials & Structures WILEY

Ductile fracture locus identification using mesoscale critical equivalent plastic strain

Haohui Xin[1] | **Milan Veljkovic**[2] | **José A.F.O. Correia**[3] | **Filippo Berto**[4]

[1]Department of Civil Engineering, School of Human Settlements and Civil Engineering, Xi'an Jiaotong University, Xi'an, China

[2]Faculty of Civil Engineering and Geosciences, Delft University of Technology, Delft, The Netherlands

[3]INEGI & CONSTRUCT, Faculty of Engineering, University of Porto, Porto, Portugal

[4]Department of Mechanical and Industrial Engineering, Norwegian University of Science and Technology (NTNU), Trondheim, Norway

Correspondence
Haohui Xin, Department of Civil Engineering, School of Human Settlements and Civil Engineering, Xi'an Jiaotong University, Xi'an, China.
Email: xinhaohui@xjtu.edu.cn

Abstract

The ductile performance of high strength steel (HSS) from different steel grades, producers, manufacturing processes varies a lot. It is also difficult to conduct all kinds of reliable experiments to generate different stress status through different initial specimen geometries or by applying different load combinations in the civil engineering sector. One of the common issues for HSS structures is to identify the parameters of the ductile fracture model conveniently from the uniaxial stress–strain relationship obtained from common coupon specimens. An attempt is made in this paper to use the proposed mesoscale critical equivalent plastic strain (MCEPS) to calibrate the fracture locus of the uncoupled phenomenological model based only on the engineering stress–strain relationship. The proposed method is successfully validated by the Sandia fracture challenge in 2014.

KEYWORDS

computational homogenization, ductile fracture, mesoscale index, nonlinear finite element simulation

1 | INTRODUCTION

The high strength steel (HSS) application in the long-span or high-rise structures is increasing because of its economical and functional advantages.[1–3] The failure prediction of HSS structures or components has drawn attention from both the academic and industrial fields. With the increasing computational ability, evaluation of the ductile fracture of HSS structures through non-linear finite element (FE) methods benefits of economical design.

The open question is how to model the ductile damage or fracture in multiaxial and non-proportional loading at the higher equivalent plastic strain. The fracture models of steels generally consist of physically based and phenomenological models. The failure of HSS is a progressive material deterioration due to the nucleation, growth and coalescence of microvoids.[4] Early physically based ductile fracture prediction is developed by analysing the evolution of cylindrical and spherical holes in a ductile matrix by McClintock[5] and Rice and Tracey.[6] Gurson[7] proposed a (porous) plasticity model that includes the void volume fraction as an internal variable. The original Gurson model is improved to consider void coalescence by Tevergaard and Needleman,[8,9] known as Gurson–Tevergaard–Needleman (GTN) model. The GTN model is further extended to consider anisotropy[10] and shear effects.[11,12] The physically based model assumed that the fracture occurs when the microvoid radius or void volume fraction reaches a critical threshold value. The phenomenological models could be further divided into the uncoupled damage model and coupled damage model.[13] In terms of the uncoupled phenomenological model,[13] the basic assumption is that the evolution of damage does not affect the effective stress–strain response of HSS before a fracture occurs. Generally, the J2 plasticity model is to be used in combination with a separate fracture model. It is assumed that the fracture

occurs at a point where a weighted measure of the accumulated equivalent plastic strain reaches a critical value,[14–16] such as the Johnson–Cook model,[17] the MMC model,[18] the Hosford–Coulomb model,[19,20] Lou–Huh model[21,22] and recent neural networks.[23,24] The critical equivalent plastic strain at the onset of fracture is the function of the stress triaxiality and the Lode (angle) parameter. In terms of the coupled phenomenological model,[13] the irreversible damage process is accounted for by the internal constitutive variables involved in the yield surface.[25–27] Generally, a damage scalar is adopted to describe the isotropic damage, and effective stress is used to describe the impact of the damage on the macrobehaviour of the materials.[27]

There is a big potential application in ductile fracture prediction of the critical components of HSS structures in the construction sector. Material parameters identification of fracture models is the first step for the failure prediction of infrastructure made of HSS. The parameters of the physically based fracture model could not be identified conveniently.[13] Although the parameters of the uncoupled phenomenological models are relatively easy to obtain, a series of experiments are needed to be conducted for each typical component to identify the parameters in the ductile fracture model. The uncoupled phenomenological models are nowadays generally used in the mechanical engineering field, especially metal forming simulation.[28,29] It is important to notice that, in mechanical engineering, the approach to design is quite different from it in civil engineering. The link between mechanical design and scientific literature is strong, probably because there is almost always an experimental validation, justified by serial production of components. Large civil structures are all different from each other, and there is no serial production. Besides, the ductile performance of HSS from different steel grades, producers, manufacturing processes (cold-formed, hot rolled, etc.) varies a lot. It is also difficult to conduct all kinds of reliable experiment to generate different stress status through different initial specimen geometries or by applying different load combinations for typical parts in the civil engineering sector, such as welds, the heat-affected zone (HAZ), bolt, headed studs and fillet corners of cold-formed tube. Hence, one of the common issues for HSS structures is to identify the parameters of the ductile fracture model conveniently from the uniaxial stress–strain relationship obtained from common coupon specimens.[30,31]

The combination of mesoscale computational homogenization triggered by the physically based model and uncoupled phenomenological model is promising to predict the ductile fracture of HSS from only the uniaxial stress–strain relationship.[32–34] The mesoscale computational homogenization method could be used to identify the fracture strain at different stress status for the calibration of the parameters of the uncoupled phenomenological model. A mesoscale failure index is generally used to link the material fracture under different multiaxial stress status. The basic assumption is that the critical value of the mesoscale failure index is kept constant under multiaxial and non-proportional loading. As mentioned earlier, the microvoid radius is proposed by Rice and Tracey in 1969[6] as the mesoscale index. However, the microvoid evolution is quite irregular, and it is relatively difficult to describe the microvoid evolution by the radius. The method to determine the equivalent microvoid radius is needed for the application of the radius as the failure index at the mesoscale. The void volume fraction is further adopted as the mesoscale failure index by Gurson in 1977[7] to alleviate the microvoid shape effects. The rising questions will be how to obtain the true stress and strain relationship of the matrix material without the microvoid. The crystal plasticity is a very good option to simulate the matrix behaviour, but the difficulty in parameter calibration of the slip system[35] hinders its applications in the civil engineering field. And it is also difficult to model the microvoid coalescence to identify the critical void volume fraction. Hence, an attempt is made in this paper to use the other mesoscale failure index to describe the material fracture considering the 'robustness' characteristics, namely, (1) simple enough for the numerical implementation and (2) convenient enough for parameters calibration.

In this paper, the mesoscale critical equivalent plastic strain (MCEPS) is proposed as the failure index at the unit cell level to calibrate the fracture locus of the uncoupled phenomenological model. The experimental data reported by the Sandia fracture challenge in 2014 are used to validate the proposed method. The stress–strain curve is divided into three stages: the elastic stage, the plastic stage and the coupled plastic-damage stage. The FE simulation is performed to obtain the true stress and strain curves in different stages. Computational homogenization is carried out based on the calibrated true stress and strain relationship, and the fracture equivalent plastic strain relationship between uniaxial tension, in-plane shear and plane strain tension is obtained based on the proposed MCEPS index. The fracture locus of the HSS is calibrated by comparing the FE results with experimental data. The ductile failure of the Sandia fracture challenge specimen is simulated to validate the identified fracture locus.

2 | PLASTIC FLOW STRESS

To predict the ductile fracture of HSS, this paper divided the identification process into two stages: (1) identify the

relationship between equivalent plastic strain and uniaxial true stress for the isotropic J2 plasticity model; (2) identify parameters of fracture strain under multiaxial stress states. It is assumed that the evolution of damage does not affect the uniaxial true stress–strain response of HSS before a fracture occurs.

2.1 | Specimens

All the test specimens were cut from a commercial steel plate with a measured thickness of 3.124 mm. Four specimens, two identical specimens as one group in terms of orientation, were tested to obtain the engineering stress–strain curves. The geometry of tensile coupon specimens and detailed procedures can be referred to Boyce et al.[36] The test results are shown in Figure 1.

2.2 | Calibration of plastic flow stress

The FE model and boundary condition used for the parameter calibration of the coupled plastic-damage stage are shown in Figure 2. One end is fixed, and the other end is used for the loading. The specimen was simulated by solid element C3D10 with a fixed mesh size of 0.25 mm to avoid the mesh size effects on the FE results. The quasi-static simulation is employed through the ABAQUS/EXPLICIT solver[37] with a total time of 1 s and a time interval of 1×10^{-6} s for the mass scaling. The division of the whole uniaxial stress–strain relationship is into three stages: elastic stage, plastic stage and coupled plastic-damage stage. The coupled plastic-damage stage is further decomposed into the plastic-dominated zone and the damage-dominated zone.[38] The true stress–plastic strain relationship of each stage is calibrated based on the method proposed by the authors' previous publication.[38] The comparisons between FE simulation and experimental results are shown in Figure 1. A good agreement is observed. The calibrated uniaxial true stress–strain relationship is shown in Figure 3.

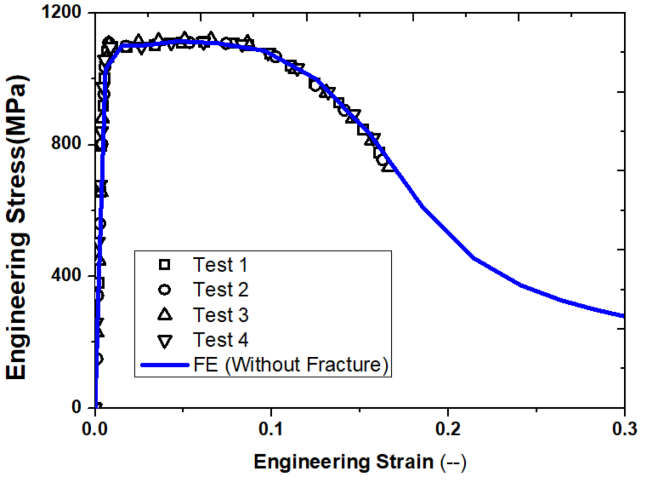

FIGURE 1 Comparisons between FE (without damage) and experimental results (experimental data are reproduced from the literature[36]) [Colour figure can be viewed at wileyonlinelibrary.com]

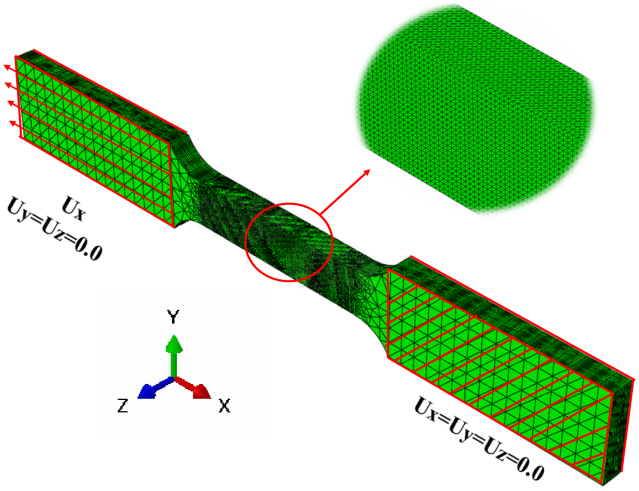

FIGURE 2 Finite element model and boundary conditions of coupon specimen [Colour figure can be viewed at wileyonlinelibrary.com]

3 | COMPUTATIONAL HOMOGENIZATION

3.1 | Unit cell and periodic boundary condition

As shown in Figure 4, the cubic with a void in the middle is assumed to be the unit cell. The volume fraction of the microvoid is related to the chemical composition of the metal. The initial void volume fraction is assumed to be 0.5%[39] referring to mild steel S355. The link between microscale and macroscale behaviour could be established based on Hill–Mandel computational homogenization method. The macroscale Cauchy stress σ_{ij} is obtained by averaging the microscale Cauchy stress, $\bar{\sigma}_{ij}$, in the unit cell domain, expressed as below[40]:

$$\sigma_{ij} = \frac{1}{|\Theta|}\int_{\Theta} \bar{\sigma}_{ij} d\Theta \tag{1}$$

Because the initial void volume fraction is quite small, the uniaxial true stress–strain curves of HSS is used as the matrix in this paper. The so-called mixed

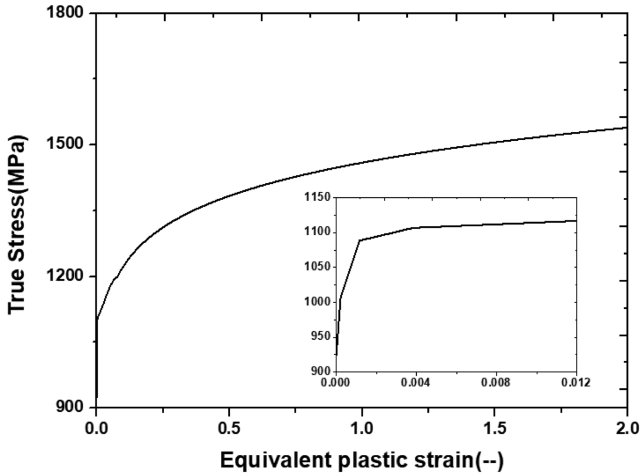

FIGURE 3 Uniaxial true stress–strain curves without considering the damage

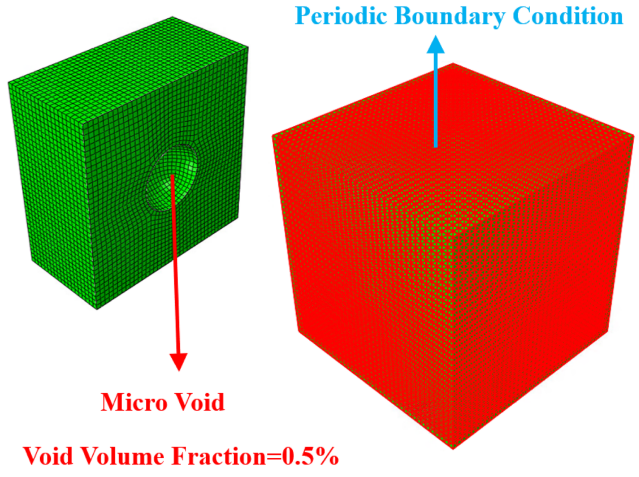

FIGURE 4 Illustration of the unit cell [Colour figure can be viewed at wileyonlinelibrary.com]

boundary conditions was implemented through the constraint equations in the ABAQUS software[37] by the following equations:

$$\int_{\partial\Theta_Y}\left(u_i^f(x,y)-\varepsilon_{ik}^c y_k\right)N_j^\Theta d\gamma_Y=0 \tag{2}$$

$$|\,u_i^f(x,y)-\varepsilon_{ik}^c y_k\,|\,N_j^\Theta \le Tol \tag{3}$$

The microvoid deformation of the unit cell under pure tension and shear is shown in Figures 5 and 6, respectively. In terms of the unit cell subjected to uniaxial tensile, the microvoid is expanded along the loading direction while the shrinkage is perpendicular to the loading direction with the tensile loading increasing. The initial sphere is gradually changed to an ellipsoid when the macro equivalent strain increased to 70.6%. In terms of the unit cell subjected to shear loading, the microvoid is expanded along 45° counterclockwise while is shrinkage along −45° counterclockwise. The micovoid deformation from the unit cell is also compared with the SEM reported in the literature.[41] A general good agreement is observed.

3.2 | Mesoscale critical equivalent plastic strain

The authors postulated that the ductile fracture of the macroscale is due to the strain concentration in the microscale. In addition to the microvoid radius mesoscale index proposed by Rice and Tracey[6] and microvoid volume fraction mesoscale index proposed by Gurson in 1977,[7] we define the MCEPS on the microvoid surface Γ_v (see Figure 4), as the mesoscale indicator (MI) to illustrate the material failure. It is assumed that the MCEPS of the unit cell is kept constant when the material is exposed to multiaxial loading. Two MIs are proposed, as expressed in Equations 4 and 5, as the MCEPS to predict the failure. MI_1 defines the homogenized equivalent strain at the microvoid surface to be the mesoscale failure index, while MI_2 defines the maximum equivalent strain at the microvoid surface to be the mesoscale failure index.

$$MI_1=\frac{1}{|\,\Gamma_v\,|}\int_{\Gamma_v}\bar{\varepsilon}^p d\Gamma \tag{4}$$

$$MI_2=\max\left(_{\Gamma_v}\bar{\varepsilon}^p\right) \tag{5}$$

The MI evolution along with the macro equivalent plastic strain is shown in Figure 7. Based on the postulation of the mesoscale failure index, the fracture strain subjected to uniaxial tension (*UT*), shear (*SH*) and plane strain tension (*PST*) is the macroequivalent plastic strain when the MCEPS of the unit cell reached the same critical value. The equivalent plastic strain with the same *MI* value is extracted from the unit cell loaded by the uniaxial tension (*UT*), shear (*SH*) and plane strain tension (*PST*), respectively, presented in Figure 8. Because the fracture strain exposed to uniaxial tension (*UT*) is not determined, the fracture strain ratio, SH to UT and also PST to UT, is plotted against the evolution of equivalent plastic strain when the fracture occurred exposed to uniaxial tension. And the relationship between strain ratio and fracture strain exposed to uniaxial strain is fitted by seven-term

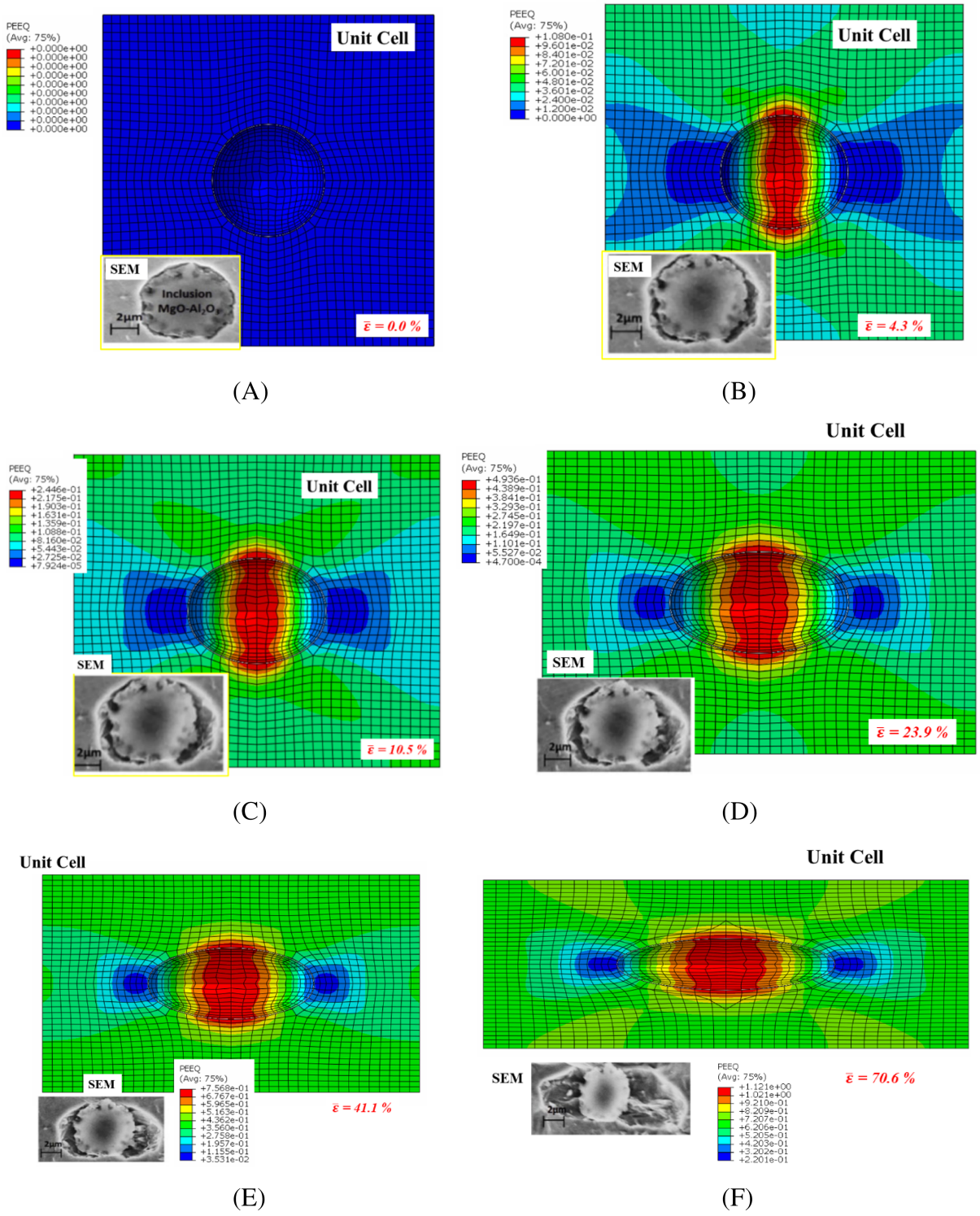

FIGURE 5 Dilation-dominated void deformation comparisons between mesoscale modelling and experimental observations (noted: SEM is reproduced from reference[41]) [Colour figure can be viewed at wileyonlinelibrary.com]

polynomial expression. The fitted coefficients are summarized in Table 1.

$$r_\chi = \sum_{i=1}^{7} \xi_i \left(\bar{\varepsilon}^p_{UT}\right)^{i-1} \quad \chi = \}SH/UT\}, \}PST/UT\} \tag{6}$$

where $r_{SH/UT}$ is the fracture strain ratio between pure shear (SH) loading and uniaxial tensile loading (UT); $r_{PST/UT}$ is the fracture strain ratio between plane strain tensile (PST) loading and uniaxial tensile (UT) loading; ξ_i is the coefficient of polynomial expression; $\bar{\varepsilon}^p_{UT}$ is the fracture strain subjected to uniaxial tension.

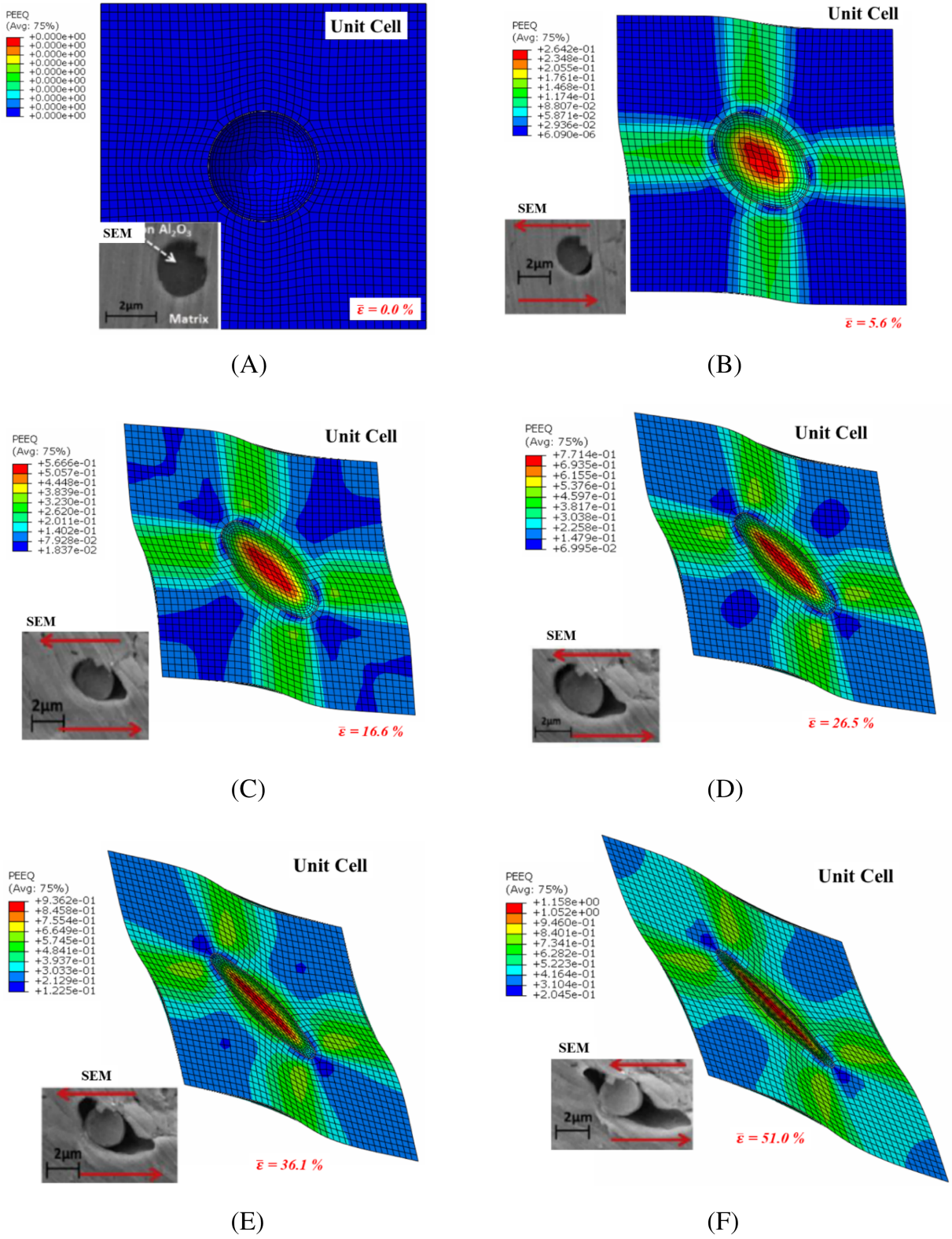

FIGURE 6 Shear-dominated void deformation comparisons between mesoscale modelling and experimental observations (noted: SEM is reproduced from reference[41]) [Colour figure can be viewed at wileyonlinelibrary.com]

4 | FRACTURE LOCUS IDENTIFICATION

The uncoupled damage model is employed to simulate the ductile fracture of HSS. The fracture locus is a function of stress triaxiality and the Lode parameter or Lode angle parameters, such as the MMC model,[18] the Hosford–Coulomb model,[19,20] Lou–Huh model[21,22] and recent neural networks.[23,24] In this paper, the Lou–Huh model,[21,22] as expressed in Equation 13, is used to identify the fracture locus.

$$\bar{\varepsilon}_f^p = C_3\left(\frac{\sqrt{\bar{L}^2+3}}{2}\right)^{C_1}\left[\frac{1}{1+C}\left(\bar{\eta}+\frac{3-\bar{L}}{3\sqrt{\bar{L}^2+3}}+C\right)\right]^{-C_2} \tag{7}$$

where $\bar{\eta}$ and $\bar{L}$ is the stress triaxiality and the Lode parameters averaged over the loading history to consider the non-proportional loading effects, as expressed in Equations 8 and 9. C is the cut-off value and is assumed to be 1/3 in this paper.

$$\bar{\eta} = \frac{1}{\bar{\varepsilon}_f^p}\int_0^{\bar{\varepsilon}_f^p} \eta d\bar{\varepsilon}^p \tag{8}$$

$$\bar{L} = \frac{1}{\bar{\varepsilon}_f^p}\int_0^{\bar{\varepsilon}_f^p} L d\bar{\varepsilon}^p \tag{9}$$

The stress triaxiality η and the Lode parameter L is given by

$$\eta = \frac{\sigma_m}{\bar{\sigma}} = \frac{\sigma_1+\sigma_2+\sigma_3}{3\bar{\sigma}} \tag{10}$$

$$L = \frac{2\sigma_2-\sigma_1-\sigma_3}{\sigma_1-\sigma_3} \tag{11}$$

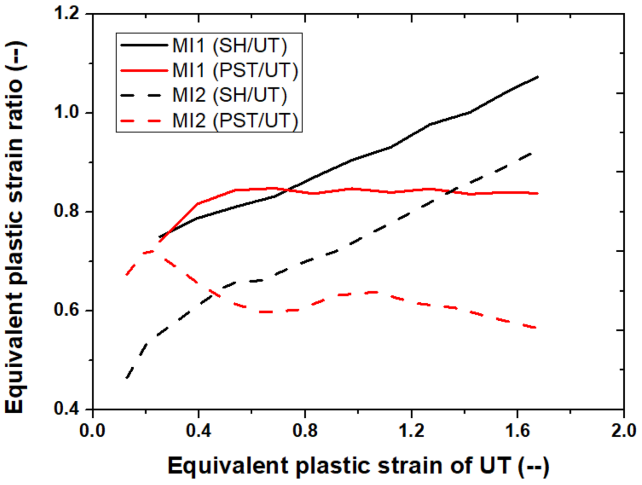

FIGURE 8 Equivalent plastic strain ratio evolution with stretching exposed to pure tension [Colour figure can be viewed at wileyonlinelibrary.com]

where $\sigma_i (i = 1,2,3)$ is the principal stress.

For uniaxial tensile (UT), $\eta = \frac{1}{3}$ and $L = -1$. For pure shear (SH), $\eta = 0$ and $L = 0$. For plane strain tension (PST), $\eta = \frac{1}{\sqrt{3}}$ and $L = 0$. Hence, the parameters of Equation 7 could be calculated based on Equations 12–14 using equivalent fracture plastic strain exposed to uniaxial tensile $\bar{\varepsilon}_{UT}^p$, exposed to shear $\bar{\varepsilon}_{SH}^p$, and exposed to plane strain tension $\bar{\varepsilon}_{PST}^p$.

$$C_1 = \log_{\left(\frac{2}{\sqrt{3}}\right)}\left[\frac{\bar{\varepsilon}_{UT}^p}{\bar{\varepsilon}_{SH}^p}\frac{\left(1/\sqrt{3}+C\right)}{\left(2/\sqrt{3}+C\right)}\right]^{-C_2} \tag{12}$$

$$C_2 = \log_{\left(\frac{1/\sqrt{3}+C}{2/\sqrt{3}+C}\right)}\left(\frac{\bar{\varepsilon}_{PST}^p}{\bar{\varepsilon}_{SH}^p}\right) \tag{13}$$

$$C_3 = \bar{\varepsilon}_{UT}^p \tag{14}$$

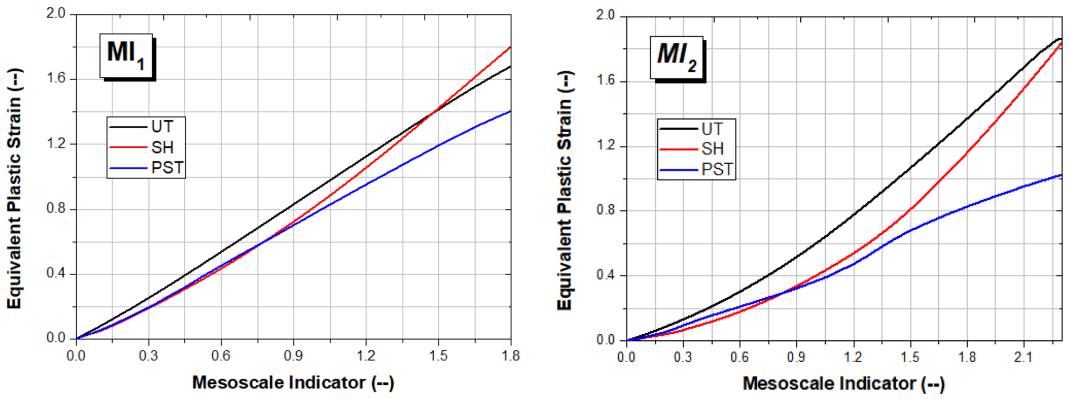

(A) (B)

FIGURE 7 Mesoscale indicator evolution along with the equivalent plastic strain [Colour figure can be viewed at wileyonlinelibrary.com]

TABLE 1 Fitted coefficients of polynomial expression in Equation 6)

Item		ξ_1	ξ_2	ξ_3	ξ_4	ξ_5	ξ_6	ξ_7
MI_1	$r_{SH/UT}$	0.4594	2.3230	−6.8023	10.4730	−8.3510	3.3340	−0.5266
	$r_{PST/UT}$	0.3185	2.8083	−5.7812	5.7804	−2.8630	0.6040	−0.0251
MI_2	$r_{SH/UT}$	0.3235	1.3663	−2.0732	1.1213	0.5242	−0.6948	0.1763
	$r_{PST/UT}$	0.3518	4.4037	−18.4010	33.0220	−29.1780	12.5330	−2.0958

The equivalent fracture plastic strain relationship, $r_{SH/UT}$, which is the ratio between shear $\bar{\varepsilon}^p_{SH}$ and uniaxial tensile $\bar{\varepsilon}^p_{UT}$, and, $r_{PST/UT}$, that is the ratio between plane strain tension $\bar{\varepsilon}^p_{PST}$ and uniaxial tensile $\bar{\varepsilon}^p_{UT}$, is already obtained based on the proposed MCEPS; see Equation 6 and Table 1. The fracture strain exposed to uniaxial tensile could be determined through the calibration by comparing the FE results against the experimental results with the ratio $r_{SH/UT}$ and $r_{PST/UT}$ obtained by the different MIs. As shown in Figures 9 and 10, the fracture strain exposed to uniaxial tension is determined to be 1.01 based on the MI_1 mesoscale failure index and 1.16 based on the MI_2 mesoscale failure index respectively, when the simulated uniform elongation reached the average value

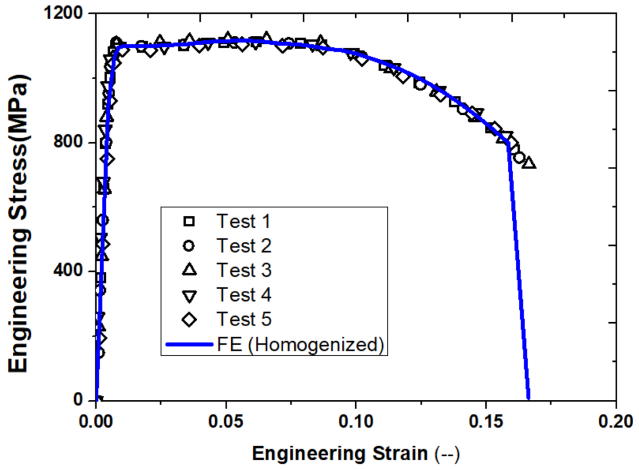

(A) Engineering stress-strain relationship

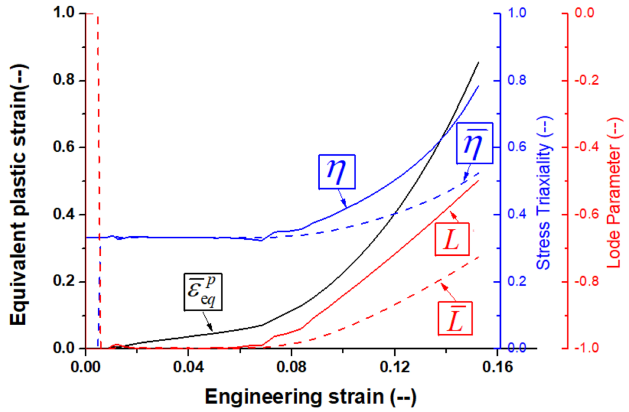

(B) Equivalent plastic strain, stress triaxiality, and Lode parameter

FIGURE 9 Calibration of fracture strain exposed to uniaxial loading using the MI_1 mesoscale failure index: A, engineering stress–strain relationship and B, equivalent plastic strain, stress triaxiality and Lode parameter [Colour figure can be viewed at wileyonlinelibrary.com]

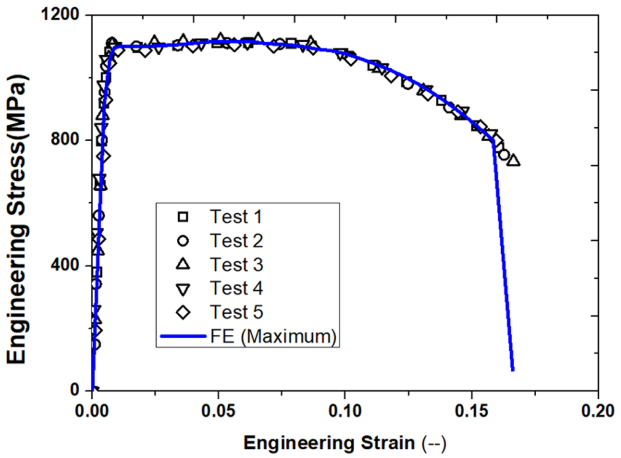

(A) Engineering stress-strain relationship

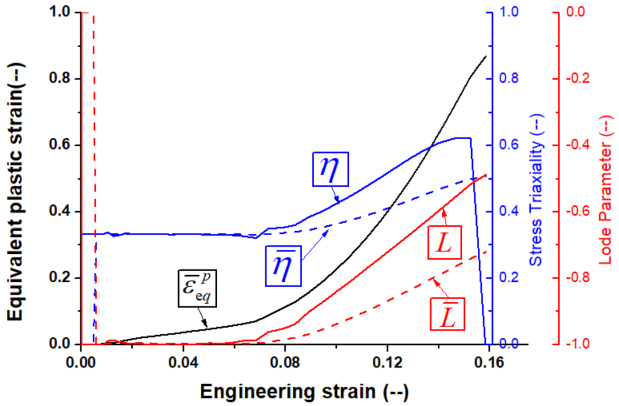

(B) Equivalent plastic strain, stress triaxiality, and Lode parameter

FIGURE 10 Calibration of fracture strain exposed to uniaxial loading using the MI_2 mesoscale failure index: A, engineering stress–strain relationship and B, equivalent plastic strain, stress triaxiality and Lode parameter [Colour figure can be viewed at wileyonlinelibrary.com]

Item	C_1	C_2	C_3	$\bar{\varepsilon}^p_{EBT}$	$\bar{\varepsilon}^p_{PST}$	$\bar{\varepsilon}^p_{UT}$	$\bar{\varepsilon}^p_{SH}$	$\bar{\varepsilon}^p_{UC}$	$\bar{\varepsilon}^p_{EBC}$
MI_1	1.141	0.163	1.010	0.98	0.84	1.01	0.91	1.26	1.20
MI_2	3.894	0.456	1.160	1.05	0.63	1.16	0.79	2.18	1.82

TABLE 2 Parameters of damage model and fracture strain at different stress status

of four coupon tests. The evolution of the equivalent plastic strain, the stress triaxiality and the Lode parameter is illustrated in Figures 9b and 10b. The results showed that the value of stress triaxiality η and the Lode parameter L is higher than the stress triaxiality averaged over the loading history $\bar{\eta}$ and the Lode parameter L averaged over the loading history. The calibrated parameters of the damage model and the fracture strains fracture exposed to uniaxial tension (*UT*), plane strain tension (*PST*), equal biaxial tension (*EBT*), in-plane shear (*SH*), uniaxial compression (*UC*) and equal biaxial compression (EBC) are listed in Table 2.

5 | VALIDATION OF FRACTURE LOCUS

The ductile fracture process of the Sandia fracture challenge specimen[36] is simulated to validate the identified fracture locus based on the proposed MCEPS failure index. The dimensions of the fracture challenge specimen can be referred to Boyce et al.[36] The FE model and boundary conditions of the fracture challenge specimen are illustrated in Figure 11. The specimen was simulated by solid element C3D10 with a fixed mesh size of 0.25 mm of the critical area to avoid the mesh size effects on the FE results.

The force-COD comparison between FE simulation and experimental results is shown in Figure 12. A good agreement is observed for both fracture locus. The fracture locus calibrated using MI_2 as the MI showed a better prediction of the force-COD relationship when the COD

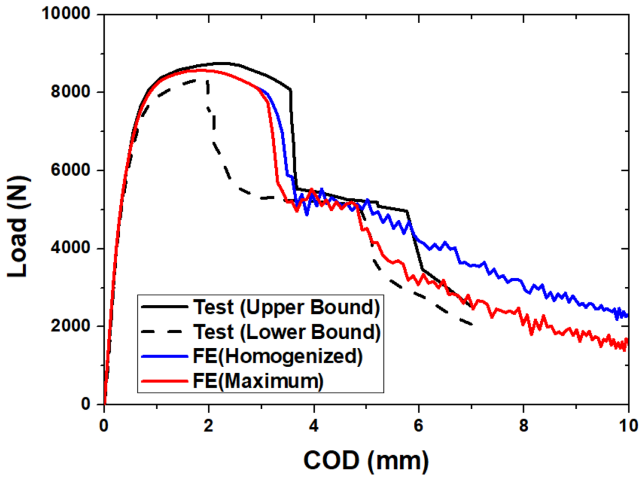

FIGURE 12 Force-COD comparison between FE simulation and experimental results [Colour figure can be viewed at wileyonlinelibrary.com]

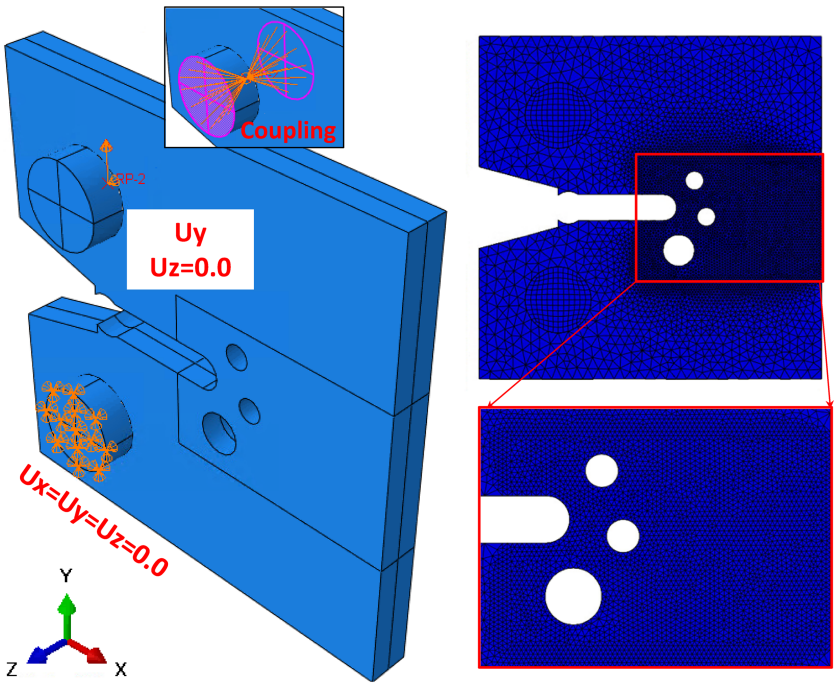

FIGURE 11 Finite element model and boundary conditions of fracture challenge specimen [Colour figure can be viewed at wileyonlinelibrary.com]

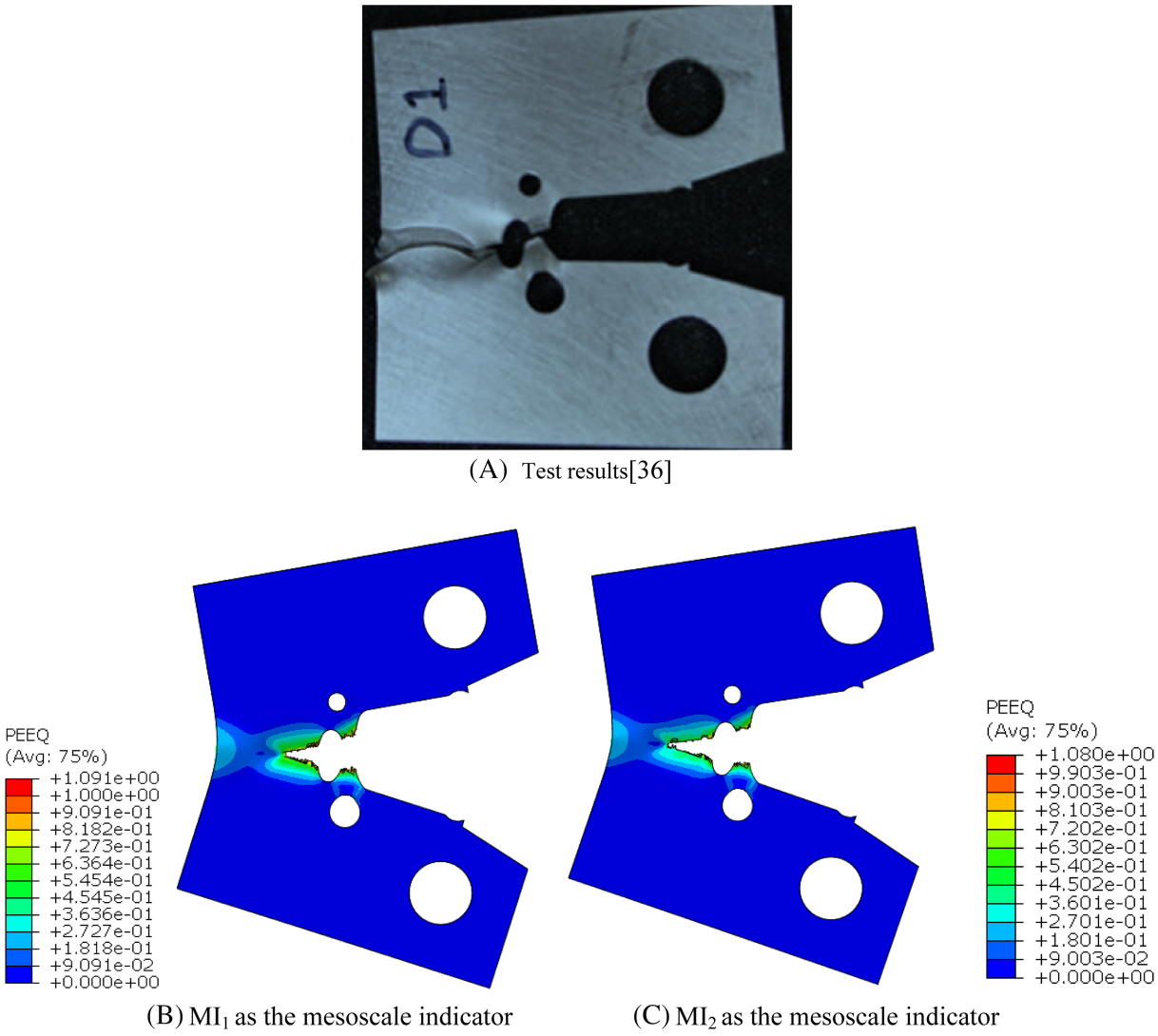

FIGURE 13 Failure mode comparisons between FE and experimental results: A, test results,[36] B, MI_1 as the mesoscale indicator and C, MI_2 as the mesoscale indicator [Colour figure can be viewed at wileyonlinelibrary.com]

is between 5.0 and 7.0 mm. Figure 13 presented the failure mode comparison between FE simulation and experimental observations. A good agreement is also observed for both fracture locus. Noted that, in terms of the failure mode of the fracture challenge specimen, the experimental force-COD relationship is close to the upper bound.

The failure mode and COD comparisons during the loading between FE simulation and experimental results are presented in Figure 14. The fracture is initiated at the inner side of the first hole when the COD increased to 3.21 mm for MI_1 fracture locus and 2.94 mm for MI_2 fracture locus. The crack is propagated to the side surface of the first hole when the COD increased to 3.58 mm for MI_1 fracture locus and 2.40 mm for MI_2 fracture locus. The crack is initiated at the opposite inner side of the first hole when the COD increased to 4.05 mm for both MI_1 fracture locus and MI_2 fracture locus. The FE simulation is generally agreed well the experimental observations.

6 | CONCLUSION AND FUTURE PLAN

Large civil structures are all different from each other and there is no serial production. It is difficult to conduct all kinds of the reliable experiment to generate different stress status through different initial specimen geometries or by applying different load combinations for typical parts in the civil engineering sector. An attempt is made to identify the parameters of the ductile fracture model conveniently from the uniaxial stress–strain relationship. The following conclusions are drawn:

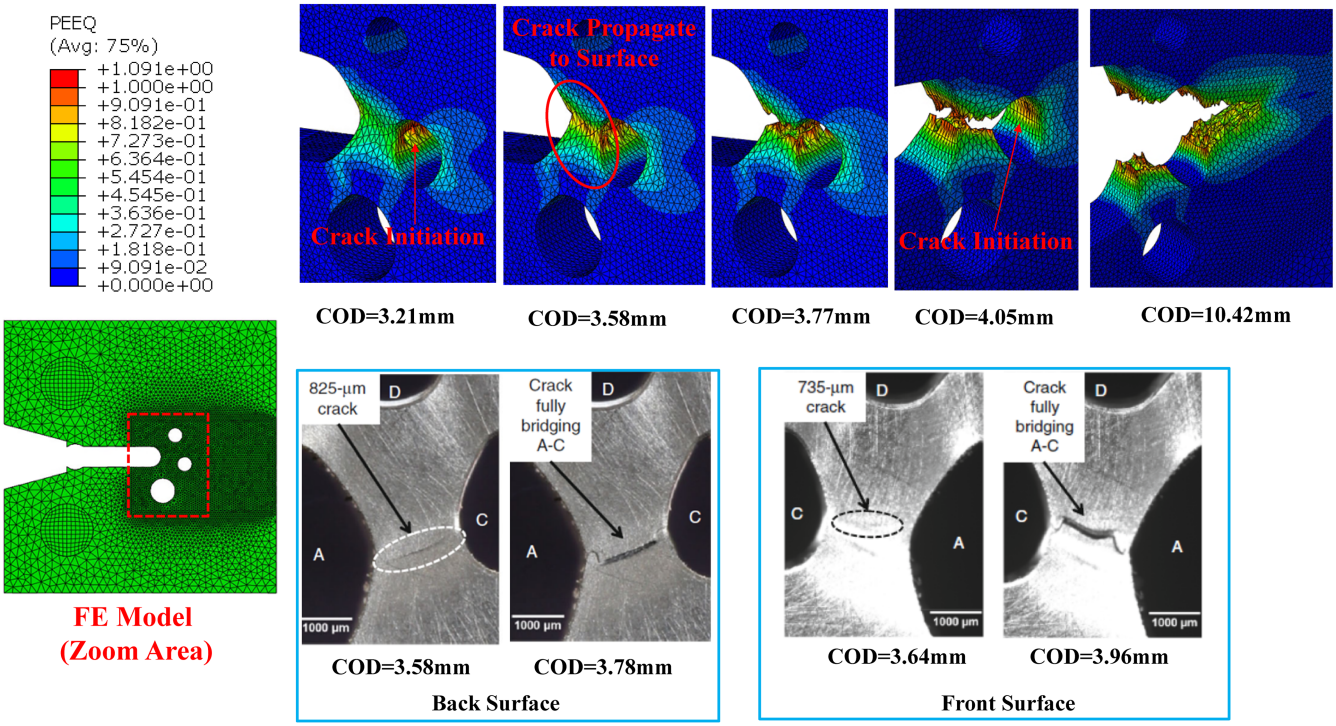

(A) MI_1 as the mesoscale indicator

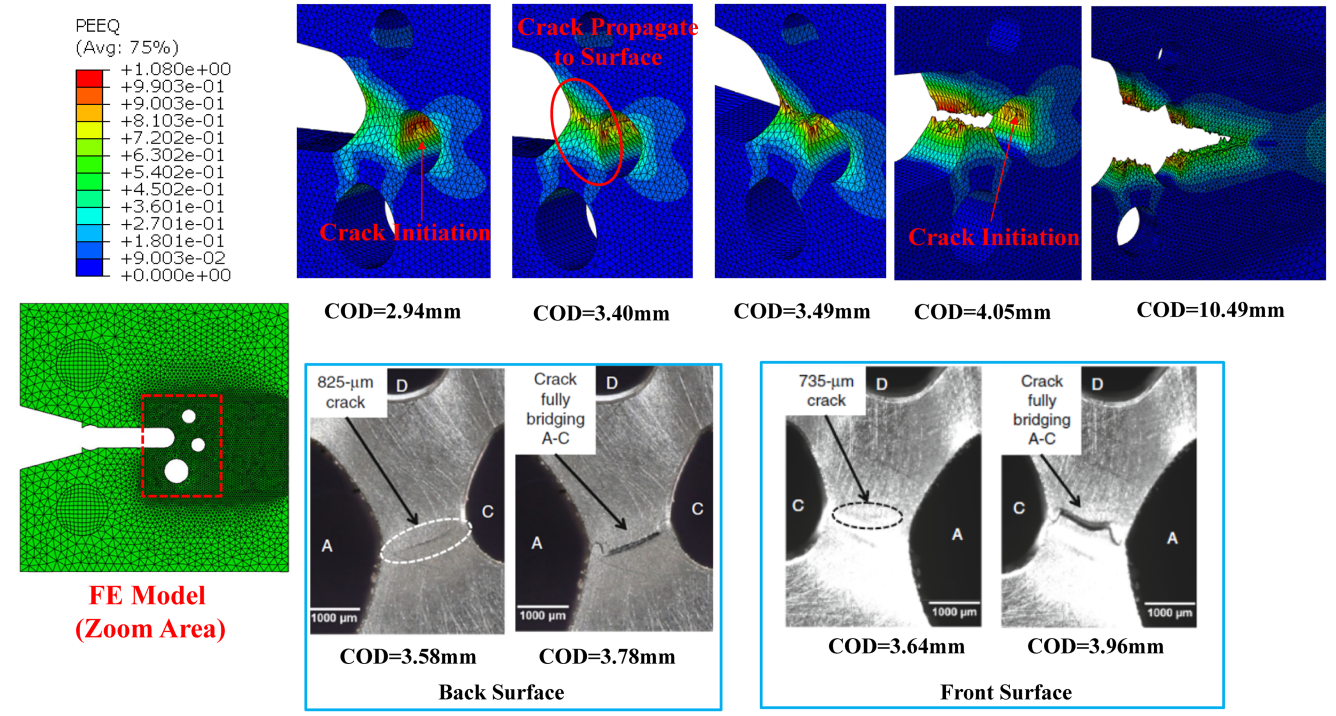

(B) MI_2 as the mesoscale indicator

FIGURE 14 Failure mode and COD comparisons during loading between FE simulation and experimental results (failure photos are reproduced from Boyce et al.[36]): A, MI_1 as the mesoscale indicator and B, MI_2 as the mesoscale indicator [Colour figure can be viewed at wileyonlinelibrary.com]

1. The MCEPS on the microvoid surface is proposed as the MI to illustrate the material failure exposed to different multiaxial stress status.
2. The ductile fracture process of the Sandia fracture challenge specimen is simulated to validate the identified fracture locus based on the proposed MCEPS failure index. The results showed that the maximum MCEPS contributes to a better prediction compared to the homogenized MCEPS. Noted that further validation with different values of stress triaxiality and Lode parameter is recommended.
3. Further research is needed: (i) comparing the identified fracture strain exposed to multiaxial stress status with different uncoupled damage models, (ii) investigating the void number and positions effects on the identified fracture strain and (iii) using the proposed failure index to predict the ductile fracture of additively manufactured materials[42,43] and welded joints.[44,45]

DATA AVAILABILITY STATEMENT

Some or all data, models or code generated or used during the study are available from the corresponding author by request.

NOMENCLATURE AND ABBREVIATIONS

C	the cut-off value and is assumed to be 1/3 in this paper
$C_i (i = 1,2,3)$	the parameters of the damage model
HSS	high strength steel
L	the lode parameter
$\bar{L}$	the lode parameters averaged over the loading history
MCEPS	mesoscale critical equivalent plastic strain
N_j^{Θ}	the normal vector of the unit cell
u_i^f	the displacement vector of the microscale
x	the position vector (Coordinate) of the macroscale
y	the position vector (Coordinate) of the microscale
ε^c	the strain tensor of the macroscale
$\bar{\varepsilon}_f^p$	the fracture equivalent plastic strain
$\bar{\varepsilon}_{UT}^p$	the fracture equivalent plastic strain subjected to uniaxial tensile
$\bar{\varepsilon}_{SH}^p$	the fracture equivalent plastic strain subjected to shear
$\bar{\varepsilon}_{PST}^p$	the fracture equivalent plastic strain subjected to plane strain tensile
σ_{ij}	the macroscale Cauchy stress
$\bar{\sigma}_{ij}$	the microscale Cauchy stress
$\sigma_i (i = 1,2,3)$	the principal stress
$\bar{\sigma}$	the von-Mises stress
Θ	the domain of the unit cell
$\partial\Theta_y$	the boundary of the unit cell
Γ_v	the surface of the micro void
η	the stress triaxiality
$\bar{\eta}$	the stress triaxiality averaged over the loading history

ORCID

Haohui Xin https://orcid.org/0000-0002-6205-5248
José A.F.O. Correia https://orcid.org/0000-0002-4148-9426
Filippo Berto https://orcid.org/0000-0001-9676-9970

REFERENCES

1. Veljkovic M, Johansson B. Design of hybrid steel girders. *J Constr Steel Res*. 2004;60(3-5):535-547.
2. Xin H, Veljkovic M. Fatigue crack initiation prediction using phantom nodes-based extended finite element method for S355 and S690 steel grades. *Eng Fract Mech*. 2019;214:164-176.
3. Xin H, Correia JAFO, Veljković M. Three-dimensional fatigue crack propagation simulation using extended finite element methods for steel grades S355 and S690 considering mean stress effects. *Eng Struct*. 2020;227:111414.
4. Benzerga AA, Leblond J-B. Ductile fracture by void growth to coalescence. *Adv Appl Mech*. 2010;10:169-305.
5. McClintock FA. A criterion for ductile fracture by the growth of holes 1968, 35, 2, 363, 371.
6. Rice JR, Tracey DM. On the ductile enlargement of voids in triaxial stress fields. *J Mech Phys Solids*. 1969;17(3):201-217.
7. Gurson AL. Continuum theory of ductile rupture by void nucleation and growth: Part I—yield criteria and flow rules for porous ductile media 1977;99:2-15.
8. Tvergaard V. Influence of voids on shear band instabilities under plane strain conditions. *Int J Fract*. 1981;17(4):389-407.
9. Tvergaard V, Needleman A. Analysis of the cup-cone fracture in a round tensile bar. *Acta Metall*. 1984;32(1):157-169.
10. Benzerga AA, Besson J. Plastic potentials for anisotropic porous solids. *Eur J Mech*. 2001;20(3):397-434.
11. Nahshon K, Hutchinson JW. Modification of the Gurson model for shear failure. *Eur J Mech A, Solids*. 2008;27(1):1-17.
12. Xue L. Constitutive modeling of void shearing effect in ductile fracture of porous materials. *Eng Fract Mech*. 2008;75(11):3343-3366.
13. Cao TS. Models for ductile damage and fracture prediction in cold bulk metal forming processes: a review. *Int J Mater Form*. 2017;10(2):139-171.
14. Mohr D, Marcadet SJ. Micromechanically-motivated phenomenological Hosford–Coulomb model for predicting ductile fracture initiation at low stress triaxialities. *Int J Solids Struct*. 2015;67:40-55.
15. Bai Y, Wierzbicki T. A new model of metal plasticity and fracture with pressure and lode dependence. *Int J Plast*. 2008;24(6):1071-1096.
16. Bao Y, Wierzbicki T. On fracture locus in the equivalent strain and stress triaxiality space. *Int J Mech Sci*. 2004;46(1):81-98.
17. Johnson GR, Cook WH. A constitutive model and data for metals subjected to large strains, high strain rates and high temperatures. Proc. 7th Int. Symp. Ballist., vol. 21, The Netherlands; 1983:541-547.

18. Bai Y, Wierzbicki T. Application of extended Mohr–coulomb criterion to ductile fracture. *Int J Fract*. 2010;161(1):1-20.
19. Roth CC, Mohr D. Effect of strain rate on ductile fracture initiation in advanced high strength steel sheets: experiments and modeling. *Int J Plast*. 2014;56:19-44.
20. Marcadet SJ, Mohr D. Effect of compression–tension loading reversal on the strain to fracture of dual phase steel sheets. *Int J Plast*. 2015;72:21-43.
21. Lou Y, Yoon JW, Huh H. Modeling of shear ductile fracture considering a changeable cut-off value for stress triaxiality. *Int J Plast*. 2014;54:56-80.
22. Lou Y, Huh H, Lim S, Pack K. New ductile fracture criterion for prediction of fracture forming limit diagrams of sheet metals. *Int J Solids Struct*. 2012;49(25):3605-3615.
23. Jordan B, Gorji MB, Mohr D. Neural network model describing the temperature-and rate-dependent stress-strain response of polypropylene. *Int J Plast*. 2020;135:102811.
24. Pandya KS, Roth CC, Mohr D. Strain rate and temperature dependent fracture of aluminum alloy 7075: experiments and neural network modeling. *Int J Plast*. 2020;135:102788.
25. Chaboche J-L. Anisotropic creep damage in the framework of continuum damage mechanics. *Nucl Eng des*. 1984;79(3):309-319.
26. Lemaitre J. Local approach of fracture. *Eng Fract Mech*. 1986;25(5-6):523-537.
27. Lemaitre J, Desmorat R. *Engineering Damage Mechanics: Ductile, Creep, Fatigue and Brittle Failures*. Springer Science & Business Media; 2005.
28. Roth CC, Mohr D. Ductile fracture experiments with locally proportional loading histories. *Int J Plast*. 2016;79:328-354.
29. Dunand M, Mohr D. Hybrid experimental–numerical analysis of basic ductile fracture experiments for sheet metals. *Int J Solids Struct*. 2010;47(9):1130-1143.
30. Xin H, Sun W, Fish J. A surrogate modeling approach for additive-manufactured materials. *Int J Multiscale Comput Eng*. 2017;15:525-543.
31. Xin H, Sun WC, Fish J. Discrete element simulations of powder-bed sintering-based additive manufacturing. *Int J Mech Sci*. 2018;149:373-392.
32. Fish J, Oskay C. A nonlocal multiscale fatigue model. *Mech Adv Mater Struct*. 2005;12(6):485-500.
33. Xin H, Mosallam A, Liu Y, Veljkovic M, He J. Mechanical characterization of a unidirectional pultruded composite lamina using micromechanics and numerical homogenization. *Construct Build Mater*. 2019;216:101-118.
34. Xin H, Nijgh M, Veljkovic M. Computational homogenization simulation on steel reinforced polymer used in the injected bolted connections. *Compos Struct*. 2019;210:942-957.
35. Hu P, Liu Y, Zhu Y, Ying L. Crystal plasticity extended models based on thermal mechanism and damage functions: application to multiscale modeling of aluminum alloy tensile behavior. *Int J Plast*. 2016;86:1-25.
36. Boyce BL, Kramer SLB, Fang HE, et al. The Sandia fracture challenge: blind round robin predictions of ductile tearing. *Int J Fract*. 2014;186(1-2):5-68.
37. Abaqus V. 2019 Documentation. Dassault Syst Simulia Corp 2019;651.
38. XIn H, Veljković M. Evaluation of high strength steels fracture based on uniaxial stress-strain curves. *Eng Fail Anal*. 2021;120:105025.
39. Yan R., Xin H., Veljkovic M. Identification of GTN damage parameters as a surrogate model for S355. *Proc. 17th Int. Symp. Tubul. Struct.* 2019:582-589.
40. Fish J. *Practical Multiscaling*. Wiley; 2013.
41. Achouri M, Germain G, Dal Santo P, Saidane D. Experimental characterization and numerical modeling of micromechanical damage under different stress states. *Mater des*. 2013;50:207-222.
42. Solberg K, Wan D, Berto F. Fatigue assessment of as-built and heat-treated Inconel 718 specimens produced by additive manufacturing including notch effects. *Fatigue Fract Eng Mater Struct*. 2020;43(10):2326-2336.
43. Solberg K, Guan S, Razavi SMJ, Welo T, Chan KC, Berto F. Fatigue of additively manufactured 316L stainless steel: the influence of porosity and surface roughness. *Fatigue Fract Eng Mater Struct*. 2019;42(9):2043-2052.
44. Lepore MA, Maligno AR, Berto F. Crack closure in friction stir weldment using non-linear model for fatigue crack propagation. *Fatigue Fract Eng Mater Struct*. 2019;42(11):2596-2608.
45. Aliha MRM, Ghoreishi SMN, Imani DM, Fotoohi Y, Berto F. Mechanical and fracture properties of aluminium cylinders manufactured by orbital friction stir welding. *Fatigue Fract Eng Mater Struct*. 2020;43(7):1514-1528.

How to cite this article: Xin H, Veljkovic M, Correia JAFO, Berto F. Ductile fracture locus identification using mesoscale critical equivalent plastic strain. *Fatigue Fract Eng Mater Struct*. 2021;44:1292–1304. https://doi.org/10.1111/ffe.13429